Journal of Materials Science: Materials in Electronics (2020) 31:13261–13272
https://doi.org/10.1007/s10854-020-03878-7

Photoluminescent properties of Sm^{3+} and Tb^{3+} codoped $CaWO_4$ nanoparticles obtained by a one-step sonochemical method

N. F. Andrade Neto[1] · J. M. P. Silva[1] · R. L. Tranquilin[2] · E. Longo[2] · J. F. M. Domenegueti[3] · M. R. D. Bomio[1] · F. V. Motta[1]

Received: 30 March 2020 / Accepted: 26 June 2020 / Published online: 6 July 2020
© Springer Science+Business Media, LLC, part of Springer Nature 2020

Abstract
Luminescent materials with LED applications can have your emission color controlled by rare earth doping. In this work, Sm^{3+}- and Tb^{3+}-codoped $CaWO_4$ nanoparticles were obtained by a one-step sonochemical method. The nanoparticles were characterized by X-ray diffractogram (XRD), Raman scattering (RS) spectroscopy, The Fourier transform infrared (FTIR) spectroscopy, scanning electron microscopy (SEM), transmission electron microscopy (TEM), and visible ultraviolet spectroscopy (UV–Vis). The photoluminescent measurements were taken at room and lower temperatures for analysis of doping in emission color. The diffractograms indicate the single-phase $CaWO_4$ with the scheelite structure and it was observed a reduction in the crystallite size as the doping. SEM and TEM images indicate the formation of nanospheres for pure and samarium-doped samples, while terbium doping results in the formation of nanorods. Room temperature photoluminescence spectra indicate a blue emission for the bare and samarium-doped $CaWO_4$, while terbium doping emits at the green color. The codoping mixes the colors blue, green, and orange, indicating a potential material with white color emission.

1 Introduction

Nanoparticulate materials receive continuous attention because they have properties different from bulk materials [1]. The reduced scale favors the formation of defects in nanomaterial surfaces, increasing the energy related to them and, consequently, making the material more reactive [2]. In the literature, several synthesis methods report the obtaining of nanostructures, among which the following methods are included: sonochemical, green synthesis, hydrothermal, and coprecipitation, due to their ease of controlling the synthesis parameters [3–8]. Among these, the sonochemical method stands out because it occurs by the generation and implosion of nano-/microbubbles in the system, it causes the local temperature and pressure to increase, and it is not necessary to apply any external temperature sources [9].

The sonochemical method can be used to obtain various types of materials, such as oxides, chlorides, and sulfides [3, 10, 11]. Among this range of materials, metal tungstates XWO_4 (were X = Ca, Cu, Cd) stand out due to their high chemical and physical stability, and they can be used in various applications, such as antimicrobial, LEDs, bacterial, photocatalytic, among others [12–15]. In the study of the LEDs, it is sought materials that have emission in the region of blue, green, and red (RGB) simultaneously, thus emitting in the region of white [16, 17]. $CaWO_4$ receives attention because its matrix usually has emission in the blue or green region, depending on the synthesis methodology and the defects generated in its lattice [18]. Emission color control is normally performed by rare earth doping, which creates intermediate levels in the $CaWO_4$ lattice, causing specific emissions. Zhang et al. [19] showed the displacement of the emission color from blue to red, as the temperature and concentration of Eu^{3+} in the $CaWO_4$ lattice change. On the other hand, Li et al. [20] showed that Eu^{3+} and Yb^{3+} codoped $CaWO_4$ generates intense emissions in the green region.

Electronic supplementary material The online version of this article (https://doi.org/10.1007/s10854-020-03878-7) contains supplementary material, which is available to authorized users.

✉ N. F. Andrade Neto
netoandrade@ufrn.edu.br

[1] LSQM, Laboratory of Chemical Synthesis of Materials, Department of Materials Engineering, Federal University of Rio Grande Do Norte, UFRN, P.O. Box 1524, Natal, RN, Brazil

[2] CDMF-UFSCar, Universidade Federal de São Carlos, P.O. Box 676, São Carlos, SP 13565-905, Brazil

[3] Departamento de Física, Universidade Federal de São Carlos, São Carlos, São Paulo 13565-905, Brazil

Emission in the white region was reported by Barbosa et al. [21], who codoped the $CaWO_4$ matrix with Tb^{3+}, Eu^{3+}, and Dy^{3+}. While Cho et al. [22] synthesized Ho^{3+}, Tm^{3+}, and Yb^{3+} codoped $CaWO_4$ by citrate complex route assisted by microwave radiation to emit in the white region.

As introduced above, the emission in the white color is obtained by simultaneously adding various cations, mainly rare earth, and typically using high temperatures and synthesis times. Thus, we sought to synthesize simply and quickly, by sonoquimico method, without the need for any heat treatment, Sm^{3+}- and Tb^{3+}-doped $CaWO_4$ with photoluminescent capacity in the blue, green, and white colors. The photoluminescent properties were analyzed at room temperature as well as at sub-zero temperatures to analyze the effect of rare earth as well as the $CaWO_4$ matrix in the color emission.

2 Materials and methods

The following were used as precursor materials: calcium nitrate [$Ca(NO_3)_2{\cdot}4H_2O$—Alfa Aesar, 98%], samarium nitrate [$Sm(NO_3)_3{\cdot}6H_2O$—Synth, 99.9%], sodium tungstate ($Na_2WO_4{\cdot}2H_2O$—Synth, 99.5%), terbium oxide (Tb_4O_7—Sigma-Aldrich, 99.5%), nitric acid (HNO_3, Synth, 65%), polyvinylpyrrolidone (PVP—$(C_6H_9NO)_n$—Vetec P.M. 40.000), ammonium hydroxide (NH_4OH—Synth, 30%), and deionized water.

Initially, a solution containing 4 mmol of calcium nitrate, 20 mmol of PVP, and 40 mL of deionized water (1) and a solution containing 4 mmol sodium tungstate, 20 mmol PVP, and 40 mL deionized water (2) were prepared and kept under stirring to complete homogenization (5 min). Afterward, the solution (1) was immersed in the solution (2) and stirred for 10 min, forming a transparent solution (3). Ammonium hydroxide was added to set the pH at 10, making the solution a whitish color. Then, solution (3) was taken to a Branson 102 C ultrasonic tip (20 kHz) where it remained for 60 min. After ultrasonic treatment, the precipitate was centrifuged and washed with deionized water until pH neutralization. Finally, the powders were dried for 24 h at 100 °C.

Terbium nitrate was prepared by dissolving Tb_4O_7 in HNO_3 to solve with a concentration of 0.01337 mol L^{-1}. Samarium- and terbium-doped samples followed the same methodology, with samarium nitrate and terbium nitrate stoichiometrically added at 1 and 2 mol% proportions to calcium nitrate in solution (1). The codoped sample was performed using 0.5% samarium and 0.5% terbium and 1% samarium and 1% terbium. The mass quantities of the reagents used are shown in Table S1 (supplementary material). The pure calcium tungstate is (CW), while the doped samples were named according to doping: CW1S (1 mol% Sm), CW1T (1 mol% Tb), CW1ST (0.5 mol% Sm and 0.5 mol% Tb), CW2S (2 mol% Sm), CW2T (2 mol% Tb), and CW2ST (1 mol% Sm and 1 mol% Tb).

The powders were characterized by X-ray diffraction (Shimadzu, XRD-6000) using CuKα radiation (1.5418 Å), in which the powders were scanned from 10 to 80° using a speed of 1°/min and step of 0.02°. Rietveld refinement using the General Structure Analysis System (GSAS) program with graphical interface EXPGUI [23] was performed to analyze the rare earth (Sm^{3+} and Tb^{3+}) cations effects on the $CaWO_4$ lattice. To do so, it was used as a background, scale factor, microstructure, crystal, texture, and strain parameters for refinement. The Raman scattering (RS) spectra were recorded at room temperature in the frequency range from 100 to 1200 cm^{-1} with a resolution of 2 cm^{-1} and 64 scans, using a VERTEX 70 RAMII Bruker spectrophotometer (USA) with an Nd:YAG laser (1024 nm) and the maximum output power kept at 100 mW. The Fourier transform infrared (FTIR) technique was performed using the Shimadzu IRTracer-100 equipment, with scanning from 500 to 4000 cm^{-1}. A scanning electron microscope (SEM) was used to observe the organization of the nanoparticles. Transmission electron microscopy (TEM) and high-resolution transmission electron microscopy (HRTEM) was performed in a FEI TECNAI G2 F20 microscope operating at 200 kV. The UV–Vis spectroscopy was performed on a Shimadzu UV-2600 equipment, with a wavelength range from 200 to 900 nm and programmed for the diffuse reflectance mode. Kubelka–Munk function [24] was applied to convert reflectance data in absorbance, and the Wood and Tauc methodology [25] was used to estimate the bandgap energy (Egap). Photoluminescence spectra were acquired using 355 nm laser (Cobolt Zouk 20) for excitation. The obtained data were transmitted to the ANDOR—Kymera 193i-B1 spectrometer for data processing. The medium was cooled using Janis cryostat (CCS-150) and the procedure was performed under a 10^{-6} mbar vacuum.

3 Results and discussion

Figure 1 shows the diffractograms for the samples obtained by the sonochemical method. Figure 1b shows the magnification of the highlighted area in Fig. 1a, relative to the main peak. According to diffractograms, all the peaks refer to the ICSD 15,586 card, relative to scheelite structure with tetragonal system and space group I41/a (n.88). No secondary phases were observed. According to Fig. 1b, it was observed the displacement of the main peak (112) as the cation replacement occurs. The Sm^{3+} doping shifts the diffraction peak to larger angles, while the Tb^{3+} shifts it to smaller ones. The codoped sample presents the largest shifts for larger angles, being the most evident ones for the CW1ST sample. The displacement to larger angles is usually

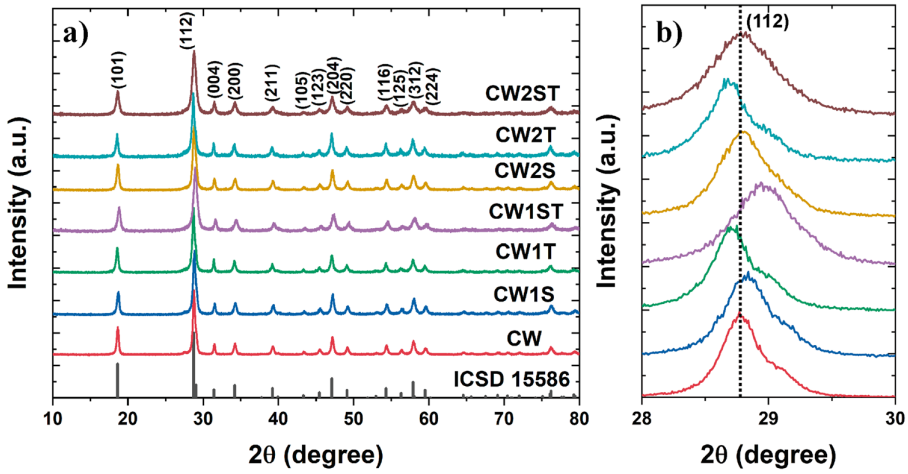

Fig. 1 **a** Diffractograms for pure and Sm^{3+}/Tb^{3+} doped $CaWO_4$ samples obtained by a sonochemical method and **b** magnification for the highlighted area

associated with the reduction in interplanar spacing, while the displacement for smaller angles is related to the increase in this spacing [26]. More information about the modifications in $CaWO_4$ lattice by Tb^{3+} and Sm^{3+} doping is studied through Rietveld refinement. The refinement was performed using a scale factor, phase fraction, Chebyshev polynomial function for background, Thomson-Cox-Hastingpseudo-Voigt peak format, changes in lattice parameters, atomic fraction coordinates, and isotropic thermal parameters as quality parameters. Figure 2a–g shows the practical (obs) and theoretical (calc) diffractograms for the $CaWO_4$ samples and Fig. 2h shows the theoretical crystal obtained by Vesta software [27]. Table 1 shows refinement data obtained by GSAS software.

According to the refinement data shown in Table 1, both dopings promote an increase in cell volume. Samarium (3+) and terbium (3+) showed an ionic radius of 0.96 and 0.92 Å, while calcium (2+) has an ionic radius of 0.99 Å. Thus, even with smaller ionic radius in comparison with Ca^{2+}, Sm^{3+} and Tb^{3+} cations have a higher valence and generate cationic vacancies for charges balancing and promoting the increase in lattice parameters [28]. On the other hand, the doping reduces the crystallite size of the $CaWO_4$ powders. Thus, it can be assumed that the defects generated by doping with rare earth ions act to alter the energy of the crystals, reducing their growth. The reduction in the crystallite size was accompanied by an increase in the microstrain of the crystalline lattice due to the presence of the different cations, as well as the defects generated by them. The $CaWO_4$ crystal illustration shown in Fig. 2h indicates that W atoms are attached to four oxygen atoms, forming the tetragonal cluster $[WO_4]$, while Ca atoms are attached to eight oxygen atoms, forming the octahedral cluster $[CaO_8]$. The small difference between theoretical and practical curves, in parallel with the low values of the refinement parameters, indicates a good quality of the refinement, making the results reliable.

Figure 3a shows the RS spectra acquired between 150 and 1200 cm^{-1} for all samples of $CaWO_4$. The presence of well-defined vibration modes indicates that the sonochemical method is efficient to obtain $CaWO_4$ with a low level of structural disorder [29]. The vibration modes in scheelite crystal can be separated into two groups, internal and external. The internal vibrations correspond to the oscillations inside the $[WO_4]^{2-}$ molecular group while internal modes correspond to the Ca^{2+} cations. The reduction in the intensity of the vibrations implies the lower occurrence of vibrations, resulting from the insertion of defects in the crystal lattice [30]. The intensity of the RS spectra is in agreement with the diffractograms, where the CW1ST sample presents a greater structural disorder. According to Fig. 3a, $CaWO_4$ has six vibration modes at 208 (A_gB_g), 330 [$v_2(A_g)$], 398 [$v_4(B_g)$], 795 [$v_3(E_g)$], 836 [$v_3(B_g)$], and 909 [$v_1(A_g)$] cm^{-1} [12]. Vibration modes $v1$ and $v2$ are associated with symmetrical elongations for W–O and O–W–O, respectively, while $v3$ and $v4$ vibration modes are associated with asymmetric elongations between W and O [31].

The linear adjustments of the v_1A_g and A_gB_g, which refer to the internal and external vibration modes were performed using the GaussAmp function in Origin software to better analyze the doping effect on the $CaWO_4$ lattice. The data obtained in Table 2 show the vibrations analyzed by FWHM, position (x_c), and area. The adjust curves are shown in Fig. S1 (supplementary material). As given in Table 2, the frequency of the A_gB_g vibration, referring to external vibrations (Ca^{2+}), was the ones that suffered the biggest alterations, indicating that doping promoted the increase in the short-range disorder of the $CaWO_4$ [32]. It is known that the level of microstructural order/disorder of small-scale materials significantly alters their properties, where the structure disorder usually favors electronic applications [33].

Figure 3b shows the Fourier transform infrared (FTIR) spectra from 500 to 4000 cm^{-1} for the pure and codoped

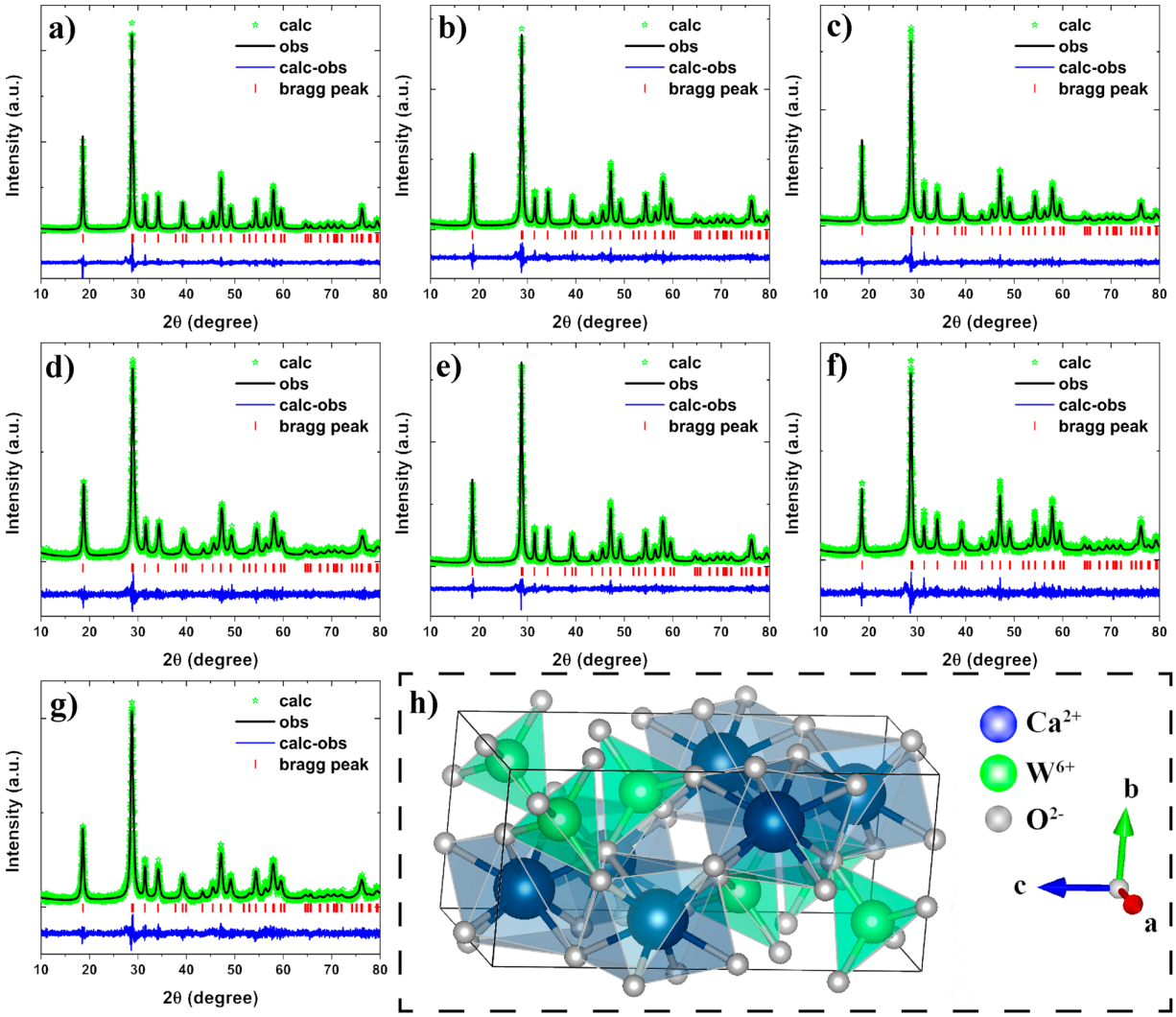

Fig. 2 practical and theoretical diffractograms obtained by Rietveld refinement for the **a** CW, **b** CW1S, **c** CW1T, **d** CW1ST, **e** CW2S, **f** CW2T, and **g** CW2ST samples and **h** illustration of $CaWO_4$ crystal

Table 1 Microstructural data and quality parameters obtained by Rietveld refinement using GSAS software

Sample	CW	CW1S	CW1T	CW1ST	CW2S	CW2T	CW2ST
a (A)	5.244	5.246	5.247	5.246	5.245	5.247	5.248
c (A)	11.378	11.381	11.384	11.385	11.379	11.383	11.381
V (A^3)	312.89	313.21	313.41	313.32	313.04	313.39	313.45
wRp	0.118	0.128	0.116	0.136	0.119	0.138	0.12
Rp	0.088	0.096	0.089	0.103	0.09	0.108	0.092
Chi^2	1.387	1.252	1.251	1.184	1.248	1.348	1.215
$R(F^2)$	0.032	0.035	0.035	0.042	0.03	0.047	0.048
∂ (nm)	27.38	23.38	24.19	16.64	22.24	21.18	15.94
ε (10^{-4})	3.14	3.69	3.55	5.2	3.87	4.05	5.39
% Sm^{3+}	–	1.16	–	0.55	2.21	–	1.02
% Tb^{3+}	–	–	1.13	0.76	–	2.36	1.86

Where ∂ = crystallite size and ε = microstrain

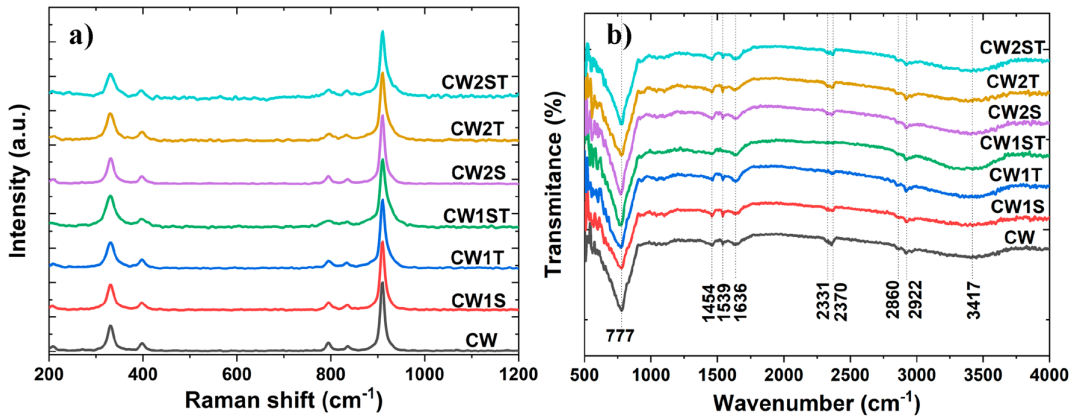

Fig. 3 **a** Raman scattering and **b** FTIR spectra for bare and doped $CaWO_4$ samples obtained by a sonochemical method

Table 2 Raman data obtained by GaussAmp function in origin software

Samples	A_gB_g			$v1A_g$		
	x_c	FWHM	Area	x_c	FWHM	Area
CW	207.46	12.04	0.028	909.83	13.30	0.618
CW1S	204.61	26.85	0.038	910.16	14.87	0.489
CW1T	209.67	14.48	0.018	910.82	16.39	0.507
CW1ST	209.29	44.39	0.039	911.37	19.65	0.241
CW2S	207.57	11.61	0.026	910.14	13.89	0.656
CW2T	207.86	15.15	0.013	910.88	18.06	0.387
CW2ST	204.67	34.77	0.048	911.98	23.89	0.531

$CaWO_4$ samples. The broadband at 3417 cm^{-1} and the smallest at 2331 and 2370 cm^{-1} refers to the hydroxyl groups (OH) present on the sample surface, probably due to the humidity of the medium [34]. The bands between 1454 and 1636 cm^{-1} are associated with H–O–H bending adsorbed at the surface of the powders. The narrow bands at 2860 and 2922 cm^{-1} are assigned to the functional groups -CH_2 and -COH, associated with residual PVP [35]. The intense peak, centered at 777 cm^{-1}, is attributed to asymmetric elongation vibration ($v3$) between O and W and O present in tetrahedron WO_4^{2-} [36]. Doping with Sm^{3+} and Tb^{3+}, possibly due to low concentrations, did not promote changes in the FTIR spectra.

Figure 4 shows the micrographs for the $CaWO_4$ samples. The micrographs indicate that the sonochemical method provides the formation of $CaWO_4$ nanoparticles in agglomerated form. These nanoparticles tend to agglomerate into micrometer-scale spheres. SEM images indicate the formation of spherical nanoparticles for the bare sample (CW). When doping $CaWO_4$ with samarium, apparent reduction of these nanospheres occurs, while terbium doping provides for the formation of nanorods. In the CW1ST sample, the morphology obtained is similar to nanoleaf, while the CW2ST sample forms nanorods. The average particle diameter was determined with the aid of the ImageJ software [37], and the methodology is shown in Fig. S2 (supplementary materials). The particle size distribution is shown in Fig. S3 (supplementary materials). According to these results, it is noticed that the samarium acts to reduce the diameter of the $CaWO_4$ nanoparticles (from 46.98 nm for CW to 32.47 nm for the CW2S sample), while the terbium, besides to modify the growth of the particles for rods, increases its average diameter (77.19 and 105.07 nm for CW1T and CW2T, respectively). According to the image highlighted in Fig. 4f, it is observed that the growth of the particles in the CW2T sample occurs oriented, indicating that the terbium acts to favor the growth in a single crystalline direction. Similar behavior was observed by Sanal Kumar et al. [38], that when doping MoO_3 with terbium in concentrations of up to 3%, they observed an increase in the size and orientation of the nanofibers.

Due to the small scale of the nanoparticles, their visualization by SEM becomes difficult. The sonochemical method is characterized by the insertion of high pressure and temperature for short periods, causing this increase to be located in the implosion regions of the bubbles generated in the process [11]. As described in the experimental methodology of this work, PVP was used as a surfactant

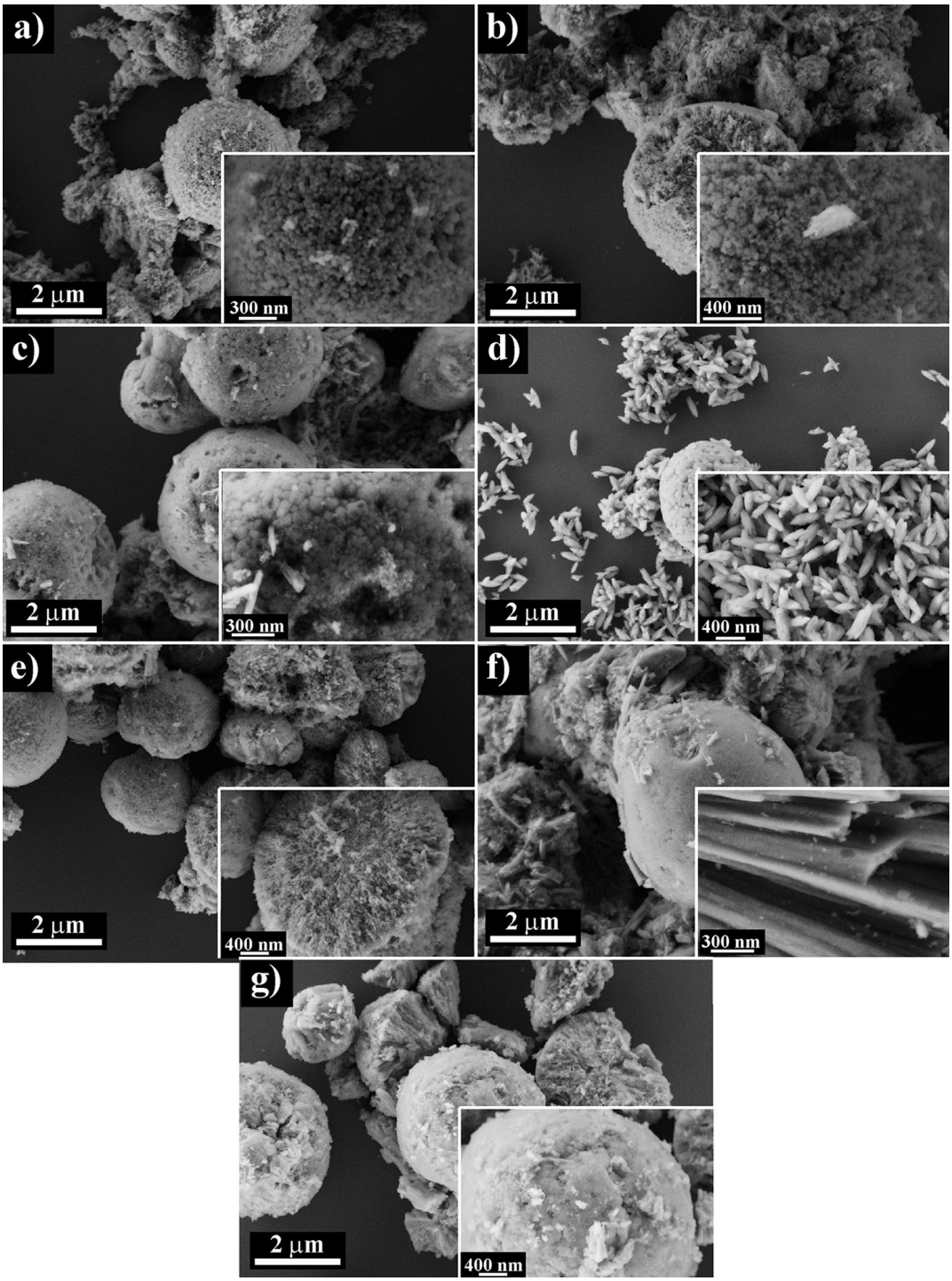

Fig. 4 SEM images for **a** CW, **b** CW1S, **c** CW1T, **d** CW1ST, **e** CW2S, **f** CW2T, and **g** CW2ST samples

in molar quantities five times higher than Ca and W cations. The use of PVP as a surfactant acts to broaden this characteristic of the sonochemical method, where the presence of its polymeric chains in the medium prevents temperature propagation, resulting in greater control of crystal growth. PVP-assisted synthesis is widely reported in the literature, avoiding agglomeration and/or control of morphology and growth [39–41].

More information about the nanoparticles was acquired by the TEM images, and is shown in Fig. 5. Figure 5a, b shows the TEM and HTEM images for the CW sample, while Fig. 5c, d for the CW2ST sample. ImageJ software was used to estimate the interplanar spacing of the samples as shown in Fig. S4 (supplementary information). The CW sample has an interplanar spacing of 0.312 nm for all particles, indicating some growth in the (112) plan, while the CW2ST sample has interplanar spacing in 0.312 and 0.479 nm referring to (112) and (101) plans. EDX analysis was performed to chemical identification in CW and CW2ST samples. The spectra are shown in Fig. S5 (supplementary material). According to spectra, both rare earths are present in the CW2ST sample, confirming that doping has occurred properly.

Figure 6a shows the absorption spectra obtained using the Kubelka–Munk function and Fig. 6b–h shows the direct transition curves according to Wood and Tauc methodology for the Egap estimation. As shown in Fig. 6a, samarium and terbium doping increases the absorption of $CaWO_4$. The increase in absorption is most evident for the codoped samples. These results are consistent with those shown in the diffractograms, being the coding responsible for major changes in the $CaWO_4$ lattice. Wood and Tauc methodology provided Egap values ranging from 4.55 to 4.75 eV, with direct transition values higher than those reported in the literature [18, 42]. Egap of polycrystalline materials is related to crystal size; very small crystals tend to have larger Egap than bulk materials [43]. Thus, the higher values of Egap, compared to the previously reported in the literature, can be attributed to the use of the PVP-assisted sonochemical method, which provided the small crystals. Also, according to the values obtained, the samarium acts to increase the $CaWO_4$ Egap, while the terbium reduces it. Moreover, even with the increase in Egap, by increasing doping from 1 to 2%, there is a slight reduction. As discussed earlier, replacing Ca^{2+} cations with Sm^{3+} and Tb^{3+} generates cationic vacancies, so it can be attributed that increasing these vacancies act to increase absorption at longer wavelengths, reducing the Egap [34].

Figure 7a–c shows the photoluminescence spectra obtained by 355 nm laser excitation at room temperature and their emission colors. According to the spectra, $CaWO_4$ (CW) has broadband with predominantly blue emission.

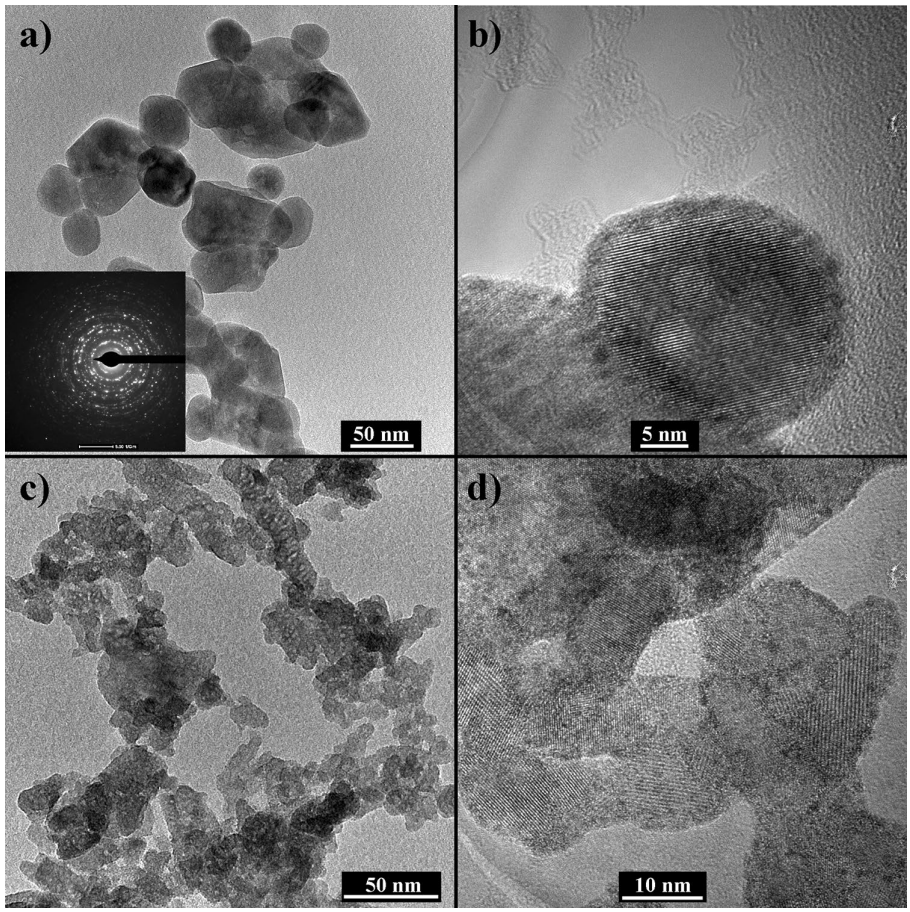

Fig. 5 TEM and HRTEM images for **a**, **b** CW and **c**, **d** CW2ST samples

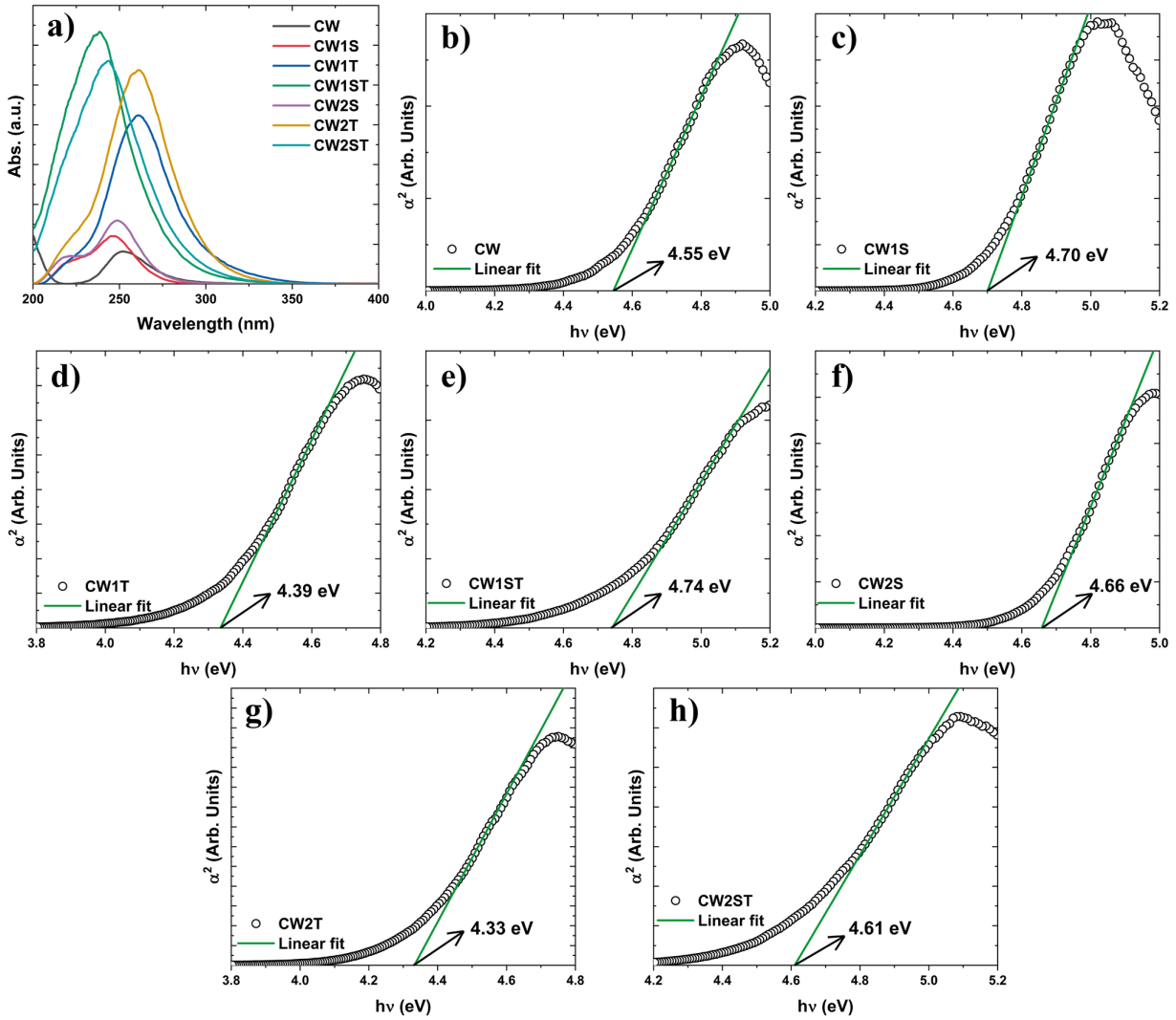

Fig. 6 **a** Absorption curves for $CaWO_4$ samples and extrapolation of the linear portion using permissible direct transition according to Wood and Tauc methodology for the Egap estimation for the **b** CW, **c** CW1S, **d** CW1T, **e** CW1ST, **f** CW2S, **g** CW2T, and **h** CW2ST samples

The CW deconvolution was performed by PeakFit software and is shown in Fig. S6 (supplementary material). $CaWO_4$ has two expected characteristic transitions $^3T_1 \rightarrow {}^1A_1$ and $^3T_2 \rightarrow {}^1A_1$, such characteristic emissions are attributed to electronic transition between W antibonding levels and oxygen (O_2p) level, characteristic of the tungstate groups [44].

Figure 7a shows the spectra for samarium-doped $CaWO_4$ samples. It can be seen the appearance of an emission band centered at 645 nm, where the variation in Sm^{3+} concentration did not change its intensity. This peak corresponds to a 4f transition of the Sm^{3+} ions, referring to $^4G_{5/2} \rightarrow {}^6H_{9/2}$ transition [45]. The appearance of this peak is consistent with the theoretical and practical emission color, indicating emission near the orange region, causing a reduction in the blue intensity of the practical emission and a shift to the right in the CIE diagram (Fig. 7d). The shift to the red region when doping with Sm is reported in some studies [46, 47].

Figure 7b shows the spectra of the terbium-doped $CaWO_4$ samples. In contrast to the samarium, increasing the concentration from 1 to 2% Tb considerably increased the characteristic emission intensity of each transition. The increase in photoluminescent intensity is associated with a higher rate of recombination of the e^-/h^+ pairs photoexcited [34]. According to the spectra, there are four characteristic transitions,

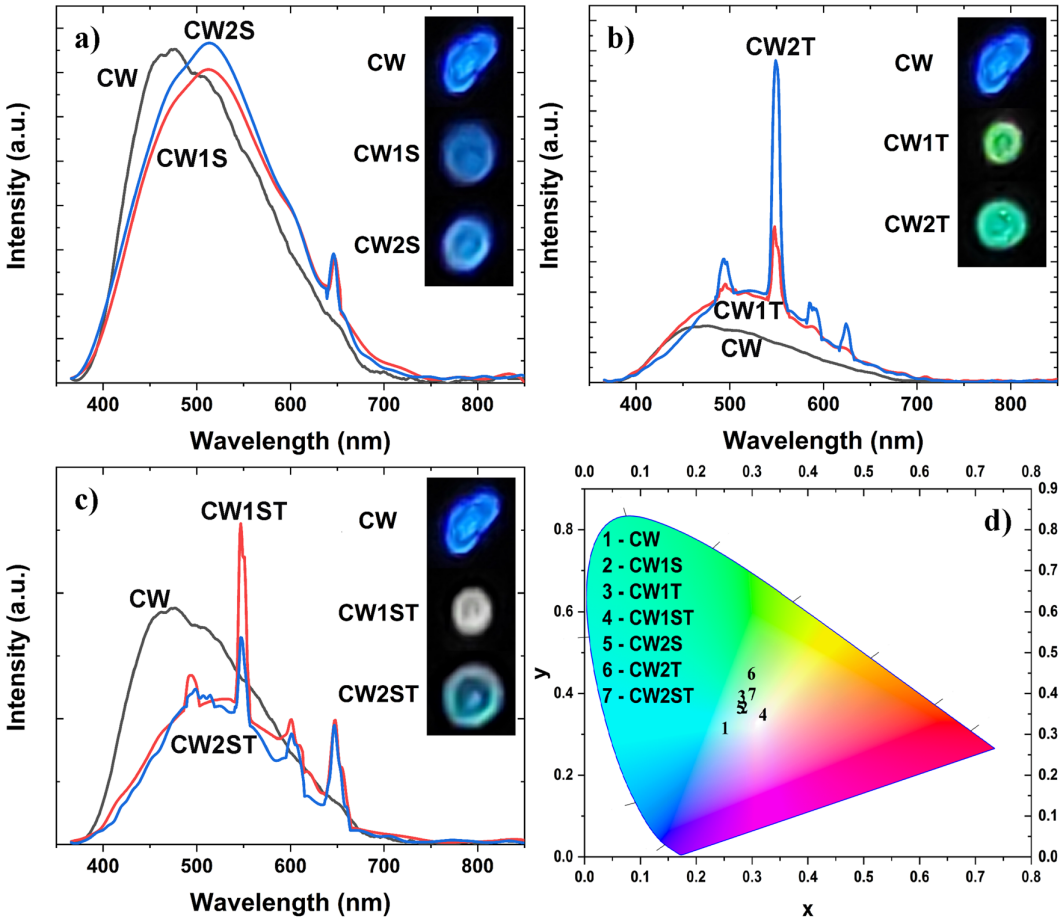

Fig. 7 Emission spectra and real color emission for **a** samarium, **b** terbium and **c** samarium- and terbium-doped $CaWO_4$ samples, and **d** CIE diagram for theoretical color emission at room temperature

located at 494, 548, 588, and 622 nm. These transitions refer to $^5D_4 \rightarrow {}^7F_6$, $^5D_4 \rightarrow {}^7F_5$, $^5D_4 \rightarrow {}^7F_4$, and $^5D_4 \rightarrow {}^7F_3$, respectively [48]. The green color, characteristic of the Tb^{3+}, is easily observed in practical color emission, were the CW2T sample has a strong green color emission. The gradient color transition (from blue to green) can be viewed on the CIE diagram (Fig. 7d).

Figure 7c shows the spectra of the samarium- and terbium-codoped $CaWO_4$ samples. According to this spectrum, it is noticed the presence of four emission bands, centered at 494, 548, 588, and 645 nm. The first three refer to $^5D_4 \rightarrow {}^7F_6$, $^5D_4 \rightarrow {}^7F_5$, and $^5D_4 \rightarrow {}^7F_4$ terbium transition, while the fourth refers to $^4G_{5/2} \rightarrow {}^6H_{9/2}$ samarium transition [45, 48]. The presence of the transition regarding the two cations confirms the correct insertion in the $CaWO_4$ lattice. As shown above, $CaWO_4$ has a characteristic blue emission, while the samarium insertion provides an emission band close to orange, reducing its bluish color, and terbium doping emits in the green color. The codoping using materials that emit in different regions of the visible spectrum is a methodology used to achieve emission in a certain color, with white emission normally desired. Emission in white is usually obtained by simultaneously adding rare earth that emits in the RGB spectrum (red, green, and blue) [21]. According to the emission color outlined in Fig. 7c, the CW1ST sample has emission at white color while the CW2ST sample is blue/green. These results indicate that amounts greater than 0.5%Tb^{3+} favor the emission in green, while the greater amount of Sm does not present a significant difference for the red region. The emission colors are following the theoretical data presented in the CIE diagram (Fig. 7d). CIE coordinates and the correlated color are shown in Table 3. According to this table, all samples have emissions in cold colors, the pure sample being

Table 3 Chromaticity coordinates (CIE) and correlated temperature color (CCT) for the pure and doped $CaWO_4$ samples

Samples	*x*	*y*	CCT (K)	Color
CW	0.2519	0.3164	11,364	Blue
CW1S	0.2854	0.3668	7492	Blue
CW1T	0.2815	0.3935	7360	Green
CW1ST	0.3098	0.4033	6245	White
CW2S	0.2796	0.3664	7778	Blue
CW2T	0.2988	0.4499	6721	Green
CW2ST	0.3002	0.3997	6599	Blue

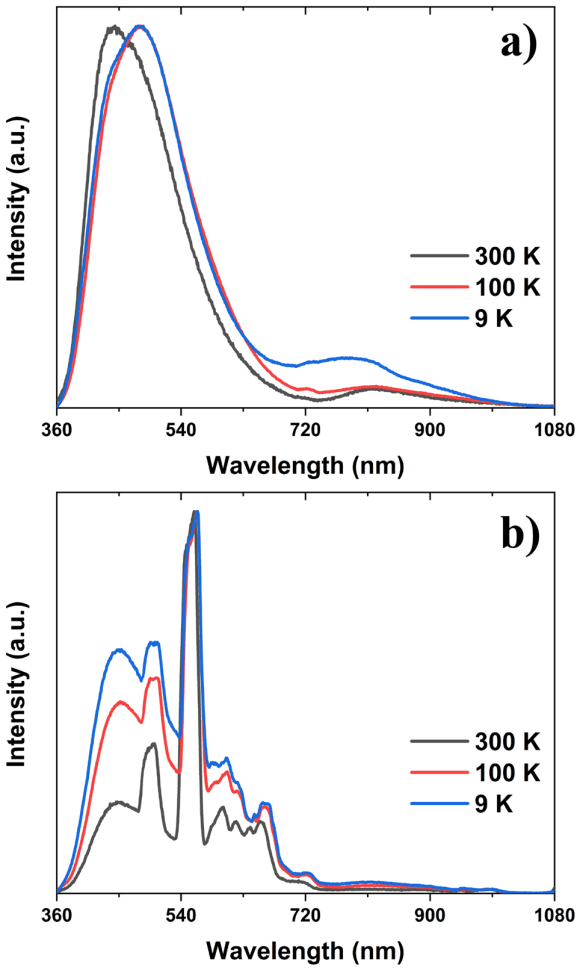

Fig. 8 PL spectra varying temperature of emission for the **a** CW and **b** CW1ST samples

colder, due to being more influenced by the blue color [49]. These color temperatures are ideal for use in indoor LEDs.

Figure 8 shows the emission spectra for the CW (Fig. 8a) and CW1ST (Fig. 8b) samples. According to Fig. 8a, as the temperature decreases from 300 to 100 K, the emission band shifts to 485 nm, where it remains unchanged as it continues to reduce the temperature to 9 K. Due to the differences in scale, it was not possible to notice the small emission band in the infrared region in Fig. 7, but the reduction in temperature has to increase. On the other hand, analyzing Fig. 8b, the reduction in temperature does not promote changes in the emission range, but significantly increases the emission intensity related to the matrix ($CaWO_4$). The temperature has no significant effect on the transitions corresponding to rare earth ions because its transition is not due to the electron of the outer orbital, but rather to the f orbitals [50]. Figure 9 shows the CIE diagram for CW and CW1ST samples. According to the diagram, the reduction in the temperature of emission generated the displacement to the green region emission for the CW sample, while for the CW1ST sample, the displacement occurs to the blue region. Thus, it can be stated that these emission color changes consist of the emission change from the $CaWO_4$ matrix, where the lowest temperatures reduce the lattice vibration, favoring the e^-/h^+ pair recombination and, consequently, the emission of the characteristic photon for the $^3T_1 \rightarrow {}^1A_1$ and $^3T_2 \rightarrow {}^1A_1$ transitions.

4 Conclusion

The sonochemical method without thermal treatment was efficient to produce pure and Sm/Tb doped $CaWO_4$ powders without secondary phases. The insertion of Sm and Tb lanthanide ions generates $CaWO_4$ lattice defects, which alter internal stresses and, consequently, reduce their periodicity, a fact observed by the reduction in the intensity of Raman spectra. These generated defects also alter the energy of the crystalline growth planes, reducing the size of the formed crystallites. The effect of the reduction on the crystallite sizes is easily visualized by the increase in Egap of powders. The $CaWO_4$ matrix presents characteristic photoemission in blue color, which is characteristic of its internal defects. As samarium is added, the blue color decreases, with the emission band appearing next to the orange one. On the other hand, the addition of terbium acts to change the emission to the green region. The emission in white was achieved by inserting the Sm and Tb cations, simultaneously in the CW1ST sample, while increasing the concentration of the dopants, the terbium prevails and the emission color shifts to green. The reduction of the emission temperature favors the matrix effect, increasing the effect of the lattice defects. The emission in the white region was obtained by mixing a simple and fast sonochemical synthesis and small amounts of dopant, making this material

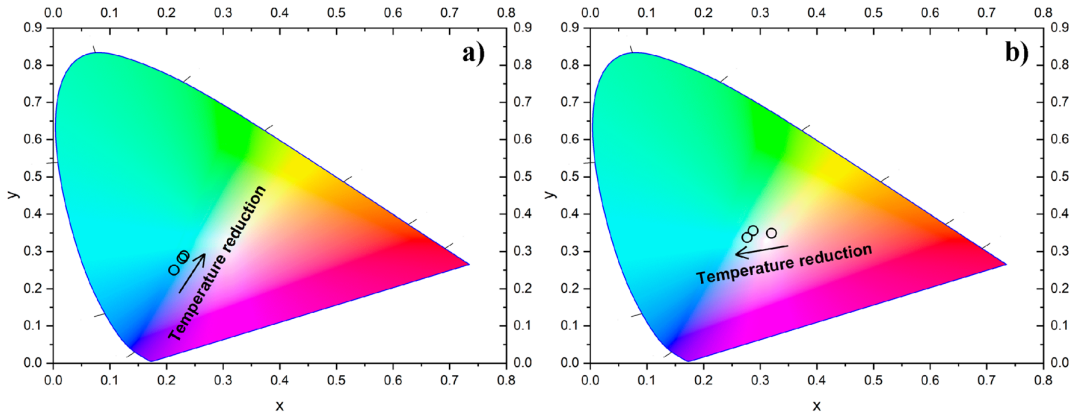

Fig. 9 CIE diagram for the **a** CW and **b** CW1ST samples varying the temperature of emission

promising for many applications, such as blue, green, and white LEDs.

Acknowledgements This study was partially financed in part by the Coordenação de Aperfeiçoamento de Pessoal de Nível Superior—Brasil (CAPES/PROCAD)—Finance Code 2013/2998/2014 and Capes Finance code 001. The authors thanks the financial support of the Brazilian research financing institution: CNPq No. 307546/2014.

References

1. N.P. Mortensen, L.M. Johnson, K.D. Grieger, J.L. Ambroso, T.R. Fennell, Reprod. Toxicol. (2019). https://doi.org/10.1016/j.reprotox.2019.08.016
2. N.F. Andrade Neto, K.N. Matsui, C.A. Paskocimas, M.R.D. Bomio, F.V. Motta, Mater. Sci. Semicond. Process. **93**, 123 (2019). https://doi.org/10.1016/j.mssp.2018.12.034
3. N.F. Andrade Neto, Y.G. Oliveira, C.A. Paskocimas, M.R.D. Bomio, F.V. Motta, J. Mater. Sci. Mater. Electron. **29**, 19052 (2018). https://doi.org/10.1007/s10854-018-0031-z
4. T. Debnath, A. Bandyopadhyay, T. Chakraborty, S. Das, S. Sutradhar, Mater. Res. Bull. **118**, 110480 (2019). https://doi.org/10.1016/j.materresbull.2019.05.005
5. M. Ghaed-Amini, M. Bazarganipour, M. Salavati-Niasari, K. Saberyan, Trans. Nonferrous Met. Soc. China **25**, 3967 (2015). https://doi.org/10.1016/S1003-6326(15)64045-6
6. D. Ghanbari, M. Salavati-Niasari, M. Esmaeili-Zare, P. Jamshidi, F. Akhtarianfar, J. Ind. Eng. Chem. **20**, 3709 (2014). https://doi.org/10.1016/j.jiec.2013.12.070
7. M.S. Ardestani, A. Bitarafan-Rajabi, P. Mohammadzadeh et al., Bioorg. Chem. **96**, 103572 (2020). https://doi.org/10.1016/j.bioorg.2020.103572
8. M.A. Ebrahimzadeh, S. Mortazavi-Derazkola, M.A. Zazouli, J. Rare Earths **38**, 13 (2020). https://doi.org/10.1016/j.jre.2019.07.004
9. N.F. Andrade Neto, Y.G. Oliveira, M.R.D. Bomio, F.V. Motta, J. Electron. Mater. **48**, 5900 (2019). https://doi.org/10.1007/s11664-019-07367-4
10. B. Souri, A. Reza Rezvani, S. Abbasi, P. Hayati, R. Centore, Inorganica Chim. Acta **498**, 119134 (2019). https://doi.org/10.1016/j.ica.2019.119134
11. N.F.A. Neto, L.M.P. Garcia, E. Longo et al., J. Mater. Sci. Mater. Electron. **28**, 12273 (2017). https://doi.org/10.1007/s10854-017-7044-x
12. J. Lv, E-c Xiao, X-h Li et al., Ceram. Int. (2019). https://doi.org/10.1016/j.ceramint.2019.10.092
13. W. Ding, X. Wu, Q. Lu, Mater. Lett. **253**, 323 (2019). https://doi.org/10.1016/j.matlet.2019.06.109
14. N.A. Shad, M.M. Sajid, N. Amin et al., Ceram. Int. **45**, 19015 (2019). https://doi.org/10.1016/j.ceramint.2019.06.142
15. F. Lei, L. Yin, Y. Shi, J. Xie, L. Zhang, L. Fan, J. Rare Earths **34**, 1179 (2016). https://doi.org/10.1016/S1002-0721(16)60151-5
16. F.F. do Carmo, J.P.C. do Nascimento, M.X. Façanha, A.S.B. Sombra, Mater. Lett. **254**, 65 (2019). https://doi.org/10.1016/j.matlet.2019.07.020
17. R. Tomala, D. Hreniak, W. Strek, J. Rare Earths **37**, 1196 (2019). https://doi.org/10.1016/j.jre.2019.03.014
18. M. Yu, H. Xu, Y. Li, Q. Dai, G. Wang, W. Qin, J. Colloid Interface Sci. **559**, 162 (2020). https://doi.org/10.1016/j.jcis.2019.10.011
19. Y. Zhang, A. Abraha, R. Zhang et al., Opt. Mater. **84**, 115 (2018). https://doi.org/10.1016/j.optmat.2018.06.062
20. L. Li, F. Qin, L. Li, H. Gao, Z. Zhang, Opt. Commun. **452**, 463 (2019). https://doi.org/10.1016/j.optcom.2019.07.077
21. H.P. Barbosa, I.G.N. Silva, M.C.F.C. Felinto, E.E.S. Teotonio, O.L. Malta, H.F. Brito, J. Alloy. Compd. **696**, 820 (2017). https://doi.org/10.1016/j.jallcom.2016.11.378
22. H. Cho, S.M. Hwang, J.B. Lee et al., Trans. Nonferrous Met. Soc. China **24**, s134 (2014). https://doi.org/10.1016/S1003-6326(14)63300-8
23. B. Toby, J. Appl. Crystallogr. **34**, 210 (2001). https://doi.org/10.1107/S0021889801002242
24. M. Patel, A. Chavda, I. Mukhopadhyay, J. Kim, A. Ray, Nanoscale **8**, 2293 (2016). https://doi.org/10.1039/C5NR06731F
25. B.D. Viezbicke, S. Patel, B.E. Davis, D.P. Birnie III, Phys. Status Solid. B Basic Res. **252**, 1700 (2015). https://doi.org/10.1002/pssb.201552007
26. N.F. Andrade Neto, Y.G. Oliveira, J.H.O. Nascimento, B.R. Carvalho, M.R.D. Bomio, F.V. Motta, J. Mater. Sci. Mater. Electron. **30**, 15214 (2019). https://doi.org/10.1007/s10854-019-01894-w
27. K. Momma, F. Izumi, J. Appl. Crystallogr. **44**, 1272 (2011). https://doi.org/10.1107/S0021889811038970
28. N.F. Andrade Neto, P. Zanatta, L.E. Nascimento, R.M. Nascimento, M.R.D. Bomio, F.V. Motta, J. Electron. Mater. **48**, 3145 (2019). https://doi.org/10.1007/s11664-019-07076-y

29. A. Phuruangrat, T. Thongtem, S. Thongtem, J. Phys. Chem. Solids **70**, 955 (2009). https://doi.org/10.1016/j.jpcs.2009.05.006
30. K.G. Sharma, N.R. Singh, J. Rare Earths **30**, 310 (2012). https://doi.org/10.1016/S1002-0721(12)60043-X
31. L.S. Cavalcante, V.M. Longo, J.C. Sczancoski et al., CrystEngComm **14**, 853 (2012). https://doi.org/10.1039/c1ce05977g
32. A. Phuruangrat, T. Thongtem, S. Thongtem, J. Cryst. Growth **311**, 4076 (2009). https://doi.org/10.1016/j.jcrysgro.2009.06.013
33. M.D.P. Silva, R.F. Gonçalves, I.C. Nogueira et al., Spectrochim. Acta Part A Mol. Biomol. Spectrosc. **153**, 428 (2016). https://doi.org/10.1016/j.saa.2015.08.047
34. N.F.A. Neto, B.P. Dias, R.L. Tranquilin et al., J. Alloy. Compd. **823**, 153617 (2020). https://doi.org/10.1016/j.jallcom.2019.153617
35. N.F. Andrade Neto, P.M. Oliveira, R.M. Nascimento, C.A. Paskocimas, M.R.D. Bomio, F.V. Motta, Ceram. Int. **45**, 651 (2019). https://doi.org/10.1016/j.ceramint.2018.09.224
36. D. Kumar, B. Singh, M. Srivastava, A. Srivastava, A. Srivastava, S. Srivastava, J. Lumin. **203**, 507 (2018)
37. C.A. Schneider, W.S. Rasband, K.W. Eliceiri, Nat. Methods **9**, 671 (2012). https://doi.org/10.1038/nmeth.2089
38. G. Sanal Kumar, N. Illyaskutty, S. Suresh, R.S. Sreedharan, V.U. Nayar, V.P.M. Pillai, J. Alloy. Compd. **698**, 215 (2017). https://doi.org/10.1016/j.jallcom.2016.11.082
39. X. Zhao, W. Zhang, R. Cao, J. Energy Chem. **26**, 1210 (2017). https://doi.org/10.1016/j.jechem.2017.08.014
40. N.F.A. Neto, T.B.O. Nunes, M. Li, E. Longo, M.R.D. Bomio, F.V. Motta, Ceram. Int. (2019). https://doi.org/10.1016/j.ceramint.2019.09.151
41. N.F. Andrade Neto, E. Longo, K.N. Matsui, C.A. Paskocimas, M.R.D. Bomio, F.V. Motta, Plasmonics **14**, 79 (2019). https://doi.org/10.1007/s11468-018-0780-9
42. C. Ayappan, B. Palanivel, V. Jayaraman, T. Maiyalagan, A. Mani, Mater. Sci. Semicond. Process. **104**, 104693 (2019). https://doi.org/10.1016/j.mssp.2019.104693
43. S.N. Sarangi, G.K. Pradhan, D. Samal, J. Alloy. Compd. **762**, 16 (2018). https://doi.org/10.1016/j.jallcom.2018.05.143
44. A. Taoufyq, V. Mauroy, T. Fiorido et al., J. Lumin. **215**, 116619 (2019). https://doi.org/10.1016/j.jlumin.2019.116619
45. X. Du, W. Huang, S. He et al., Ceram. Int. **44**, 19402 (2018). https://doi.org/10.1016/j.ceramint.2018.07.174
46. D.J. Park, T. Sekino, S. Tsukuda, A. Hayashi, T. Kusunose, S.-I. Tanaka, J. Solid State Chem. **184**, 2695 (2011). https://doi.org/10.1016/j.jssc.2011.08.012
47. C.N. Pangul, S.W. Anwane, S.B. Kondawar, Mater. Today Proc. **15**, 464 (2019). https://doi.org/10.1016/j.matpr.2019.04.108
48. C. Du, F. Lang, Y. Su, Z. Liu, J. Colloid Interface Sci. **394**, 94 (2013). https://doi.org/10.1016/j.jcis.2012.11.012
49. P.N. Medeiros, A.A.G. Santiago, E.A.C. Ferreira et al., J. Alloy. Compd. **747**, 1078 (2018). https://doi.org/10.1016/j.jallcom.2018.03.090
50. D. Kumar, B.P. Singh, M. Srivastava et al., J. Lumin. **203**, 507 (2018). https://doi.org/10.1016/j.jlumin.2018.06.065

Publisher's Note Springer Nature remains neutral with regard to jurisdictional claims in published maps and institutional affiliations.